# Intrinsically undamped plasmon modes in narrow electron bands

Cyprian Lewandowski[a,1] and Leonid Levitov[a]

[a]Department of Physics, Massachusetts Institute of Technology, Cambridge, MA 02139

Edited by Eugene J. Mele, University of Pennsylvania, Philadelphia, PA, and approved August 22, 2019 (received for review May 25, 2019)

**Surface plasmons in 2-dimensional electron systems with narrow Bloch bands feature an interesting regime in which Landau damping (dissipation via electron–hole pair excitation) is completely quenched. This surprising behavior is made possible by strong coupling in narrow-band systems characterized by large values of the "fine structure" constant $\alpha = e^2/\hbar\kappa v_F$. Dissipation quenching occurs when dispersing plasmon modes rise above the particle–hole continuum, extending into the forbidden energy gap that is free from particle–hole excitations. The effect is predicted to be prominent in moiré graphene, where at magic twist-angle values, flat bands feature $\alpha \gg 1$. The extinction of Landau damping enhances spatial optical coherence. Speckle-like interference, arising in the presence of disorder scattering, can serve as a telltale signature of undamped plasmons directly accessible in near-field imaging experiments.**

undamped plasmon excitations | Landau damping | twisted bilayer graphene

Landau damping, a process by which collective mode decays into electron–hole pairs, is often taken to be an integral attribute of graphene plasmon excitations (1–5). Here, we predict extinction of this dissipation mechanism in materials with narrow electron bands, such as twisted bilayer graphene (TBG) (6–10). Intrinsically undamped plasmons in narrow-band materials arise due to large fine structure parameter values $\alpha = e^2/\hbar\kappa v_F$: strong interactions push plasmon dispersion into the energy gap above the particle–hole (p-h) continuum as illustrated in Fig. 1. In this region, plasmons become decoupled from p-h pair excitations. Dissipation quenching, which is a surprising manifestation of strong coupling physics, is a robust effect that persists up to room temperature and is insensitive to disorder (Figs. 1 and 2). Collective charge modes, which are damping free, are of keen interest for quantum information science as a vehicle to realize dissipationless photon–matter coupling, high-Q resonators, single-photon phase shifters, and other missing components for the photon-based quantum information processing toolbox (15). Although extinction of Landau damping is a general effect present in all narrow electron bands, our analysis will focus on TBG flat bands, a system of high current interest (16–20), in which undamped plasmons can be directly probed.

Fig. 1 depicts plasmon mode for a narrow-band model that mimics the key features of the TBG band. Mode dispersion (red line) and its damping are of a conventional form at energies less than the bandwidth, $\omega \lesssim W$. At lowest energies, plasmon mode is positioned outside the p-h continuum, as expected; this suppresses the $T = 0$ Landau damping but does not protect the mode from decaying into p-h excitations through disorder scattering or from the conventional $T > 0$ Landau damping (1, 2, 21–25). At higher energies, $\omega \sim 2E_F$ (marked by arrows in Fig. 1), the mode plunges into p-h continuum and is Landau damped at $2E_F \lesssim \omega \lesssim 2W$, even at $T = 0$. However, an interesting change occurs after the mode rises above the p-h continuum. In the forbidden gap region, $\omega > 2W$, it becomes damping free, since at these energies, there are no free p-h pairs into which plasmon could decay. This behavior is manifest in the $T$ dependence of the resonances, which are washed out with increasing temperature at $\omega \lesssim W$ but remain sharp at $\omega > W$, even at $T \sim E_F$ (Fig. 1 *B* and *C*).

As we will see, mode dispersion has a square root form characteristic of 2-dimensional (2D) plasmons (26, 27),

$$\omega_{\rm p}(q) = \sqrt{\beta_q q}, \qquad [1]$$

with a weak $q$ dependence in $\beta_q$ (Eq. **14**). This expression, however, is valid not just at low energies, $0 < \omega \lesssim W$, but also at higher energies, $\omega \gg W$, where the mode is undamped. While the dispersion in Eq. **1** is of the conventional 2D plasmon form, we emphasize that here it takes on a different role, as it describes the plasmon mode at frequencies much higher than the carrier bandwidth, extending to

$$\omega_{\rm p} \sim \sqrt{\alpha} W \gg W, \quad \alpha \sim 20 - 30, \qquad [2]$$

where the high-$\alpha$ values correspond to flat bands in magic-angle moiré graphene. Also, unlike the conventional plasmons, the dispersion in Eq. **1** is not limited to longest wavelengths. Indeed, as illustrated Fig. 1*A*, it extends to fairly high wavenumbers on the order of the mini Brillouin zone size.

The wavelengths of these plasmons are only 2 to 3 times greater than the moiré superlattice period. Such short wavelengths are of considerable interest for plasmonics and are within resolution of the state-of-the-art scanning near-field microscopy techniques (4, 5) (currently as good as 10 nm [28, 29]). In addition to measuring plasmon dispersion, these

## Significance

**We argue that moiré graphene provides an opportunity to realize plasmons not subject to Landau damping. Eliminating damping is central for the ongoing quest for low-loss plasmons and dissipationless light–matter coupling. "Lifting the curse" of Landau dissipation is a surprising behavior originating from plasmon modes extending far above the narrow-band particle–hole continuum into the forbidden energy gap, where they decouple from particle–hole excitations. While our findings apply broadly to all narrow electron bands with an energy gap above the flat band, these effects are particularly prominent in moiré graphene because of uniquely strong electron interactions in this material. The intrinsically undamped plasmons feature enhanced optical coherence and spatial interference, directly testable by state-of-the-art near-field techniques.**

Author contributions: C.L. and L.L. designed research, performed research, analyzed data, and wrote the paper.

The authors declare no conflict of interest.

This article is a PNAS Direct Submission.



[1]To whom correspondence may be addressed. Email: cyprian@mit.edu.

This article contains supporting information online at www.pnas.org/lookup/suppl/doi:10.1073/pnas.1909069116/-/DCSupplemental.

First published September 27, 2019.

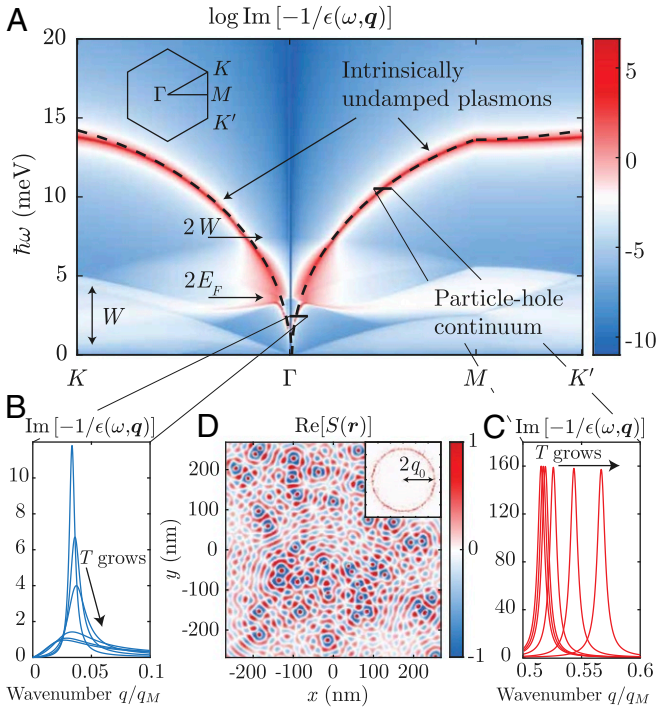


**Fig. 1.** (*A*) Electron loss function $\mathrm{Im}\,(-1/\varepsilon(\omega,\boldsymbol{q}))$ for a narrow-band toy model (the hexagonal tight-binding model) (Eq. **10**). Parameter values are chosen to mimic TBG bands (bandwidth $W = 3.75$ meV, lattice periodicity $L_M = 13.4$ nm, Fermi energy in the conduction band at $E_F \approx 1.81$ meV); log scale is used to clarify the relation between different features. Arrows mark the interband p-h continuum edges. Plasmon dispersion (red line) is fitted with $\omega_p(q) = \sqrt{\beta_q q}$ (Eq. **1**) (dashed line). The difference between Landau-damped (*B*) and undamped (*C*) behavior is illustrated by line cuts of plasmon resonances at the locations marked in *A* taken at temperatures $T/E_F = 0, 0.075, 0.1, 0.2, 0.3, 0.4$. Resonances broaden with $T$ in *B* and are $T$ independent in *C* (the residual resonance width models extrinsic damping due to phonons and disorder [11–14]). Resonances at the 3 lowest $T$ values in *C* are slightly offset for clarity. (*D*) Speckle pattern in scanning near-field microscopy signal (4, 5) $S(\boldsymbol{r})$ (Eq. **3**) due to undamped plasmons; optical coherence is manifest in Fourier spectrum $|S_{\boldsymbol{k}}|^2$ (*Inset*). Results shown are for plasmon momentum $q_0 = q_M/2 \approx 0.14$ nm$^{-1}$, where $q_M$ is the distance between points *M* and Γ, and disorder is modeled as 40 randomly placed point defects.

techniques can be used to directly visualize the qualitative change in the damping character and strength. Enhanced optical coherence will manifest itself in striking speckle-like interference as illustrated in Figs. 1*D* and 2.

Indeed, because of the absence of Landau damping at the energies of interest, $\omega > W$, and also because these energies are smaller than carbon optical phonon energies, the dominant dissipation mechanism is likely to be elastic scattering by disorder. At low energies, where plasmon mode coexists with p-h continuum, disorder scattering merely assists Landau damping, allowing plasmons to decay into p-h pairs by passing some of their momentum to the lattice. However, at the energies above p-h continuum, $\omega > W$, since the decay into pairs is quenched, disorder will lead to predominantly elastic scattering among plasmon excitations. Such scattering preserves optical coherence and is expected to produce speckle patterns in spatial near-field images as illustrated in Fig. 1*D*.

To model this behavior, we consider the signal $S(\boldsymbol{r})$ excited by the scanning tip and measured at the same location. Monochromatic plasmon excitation at energy $E$ is scattered by impurities or defects and on returning to the tip, produces signal

$$S(\boldsymbol{r}) = J_0 \int d^2\boldsymbol{r}'\, G_E(\boldsymbol{r}-\boldsymbol{r}')\eta(\boldsymbol{r}')\, G_E(\boldsymbol{r}'-\boldsymbol{r}), \qquad [3]$$

where $\eta(\boldsymbol{r})$ is the disorder potential, $J_0$ is excitation amplitude, and $G_E(\boldsymbol{r})$ is the Green's function of the plasmon excitation (*SI Appendix*, section 1). The spatial signal (Fig. 1*D*) exhibits a characteristic speckle pattern familiar from laser physics. In graphene plasmonics, speckle-like interference provides a direct manifestation of optical coherence enhancement in the absence of Landau damping. Accordingly, the Fourier transform of the image, $S_{\boldsymbol{k}} = \int d^2 r S(\boldsymbol{r}) e^{-i\boldsymbol{k}\boldsymbol{r}}$, yields power spectrum $|S_{\boldsymbol{k}}|^2$ that features a ring-like structure; the ring radius is $k = 2q_0$, where $q_0$ is the plasmon excitation wavenumber (Fig. 1*D*, *Inset*). Simple calculation, described in *SI Appendix*, section 1, predicts power spectrum that sharply peaks at the ring:

$$|S_{\boldsymbol{k}}|^2 \sim \frac{|\eta_{\boldsymbol{k}}|^2}{|k^2 - 4(q_0 - i\delta)^2|}, \qquad [4]$$

where $\delta$ is a parameter characterizing extrinsic damping due to phonon scattering and other inelastic processes. In the fully coherent regime ($\delta = 0$), the quantity $|S_{\boldsymbol{k}}|^2$ exhibits a power law singularity at the ring, $k = 2q_0$. As the amount of incoherent scattering increases, the peak is gradually washed out. This behavior is illustrated in Fig. 2.

We note that recent work (19) analyzed interband plasmon excitations in TBG, which are dominated by polarization of the bands above the flat band and are distinct from the flat-band plasmons analyzed here. Recent experiments (20) reported observation of plasmons in TBG; however, their appeal for constructing intrinsically protected collective modes remained unnoticed in graphene literature. Also, plasmons in narrow bands were analyzed in the context of high-$T_c$ superconductivity (30), finding that plasmon mode can rise above the flat band. However, in cuprates, unlike moiré graphene, the narrow band is not separated from higher bands by a forbidden energy gap, and thus,

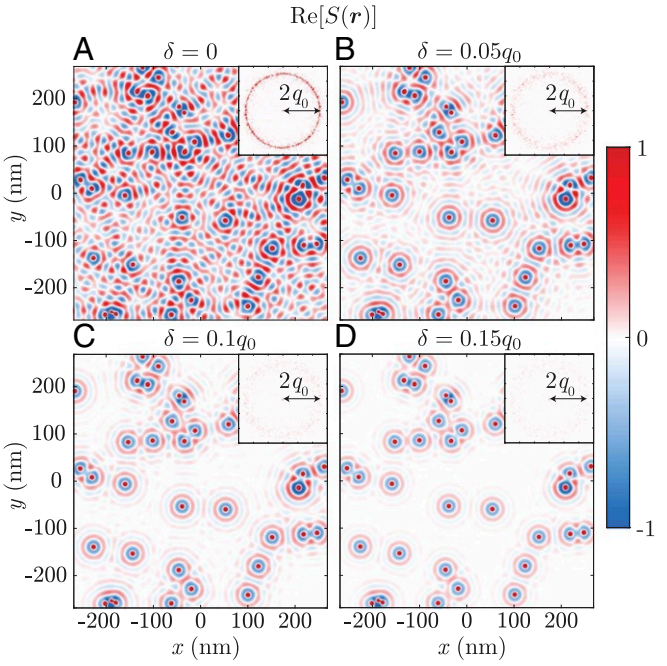


**Fig. 2.** (*A–D*) Speckle patterns arising due to optical coherence of undamped plasmons in scanning near-field microscopy signal $S(\boldsymbol{r})$ (Eq. **3**) at various ratios of the incoherent to coherent damping $\delta/q_0$. *Insets* show the corresponding square of the speckle pattern's Fourier transform amplitude $|S_{\boldsymbol{k}}|^2$. In all panels, for clarity of comparison, we set the plasmon momentum as in Fig. 1*D* ($q_0 = q_M/2 \approx 0.14$ nm$^{-1}$) and vary only the ratio $\delta/q_0$. The disorder is taken as 40 randomly placed Dirac delta functions.

the mode studied in ref. 30 will plunge into a higher band before acquiring an undamped character.

Next, we present analysis of the hexagonal-lattice toy model that mimics the key features of Landau-damped and intrinsically undamped modes in TBG. The hexagonal-lattice tight-binding model possesses the same symmetry and the same number of subbands as the flat band in TBG. We match the energy and length scales by choosing the width of a single band $W$ and the hexagonal lattice period $L_M$ identical to the parameters in TBG: $W=3.75$ meV, and $L_M=a/2\sin(\theta/2)$ is the moiré superlattice periodicity. For the magic angle value $\theta=1.05^\circ$, using carbon spacing $a=0.246$ nm, this gives $L_M=13.4$ nm. To ensure that a unit cell of the toy model can accommodate 4 electrons just as the moiré cell does in TBG, we make the toy model 4-fold degenerate. Comparison with plasmons for the actual TBG model, presented below, will help us to identify the features that are general as well as those that are a specific property of TBG.

Our nearest neighbor tight-binding Hamiltonian is

$$H_{\rm toy}=\begin{pmatrix}0 & h_{\boldsymbol{k}}\\ h_{\boldsymbol{k}}^* & 0\end{pmatrix},\quad h_{\boldsymbol{k}}=\frac{W}{3}\sum_{\boldsymbol{e}_j}e^{i\boldsymbol{k}\cdot\boldsymbol{e}_j}, \qquad [5]$$

with the hopping matrix element $W/3$ to nearest neighbors at positions $\boldsymbol{e}_j=(\cos(2\pi j/3),\sin(2\pi j/3))L_M/\sqrt{3},\ j=0,1,2$. Here, $W$ is the bandwidth measured from Dirac point, and the nearest neighbor distance $L_M/\sqrt{3}$ is chosen such that the lattice period of the hexagonal toy model matches the moiré superlattice period. Corresponding energies $E_{s,\boldsymbol{k}}$ and eigenstates $\Psi_{s,\boldsymbol{k}}$ are then

$$E_{s,\boldsymbol{k}}=s|h_{\boldsymbol{k}}|,\quad \Psi_{s,\boldsymbol{k}}=\frac{1}{\sqrt{2}}\begin{pmatrix}se^{i\varphi_{\boldsymbol{k}}}\\ 1\end{pmatrix}, \qquad [6]$$

where $\varphi_{\boldsymbol{k}}=\arg\ h_{\boldsymbol{k}}$ and the band index $s=\pm$ labels the conduction and valence band.

Plasmons can be obtained from the nodes of the complex dielectric function, describing the dynamical response of a material to an outside electric perturbation:

$$\varepsilon(\omega,\boldsymbol{q})=1-V_{\boldsymbol{q}}\Pi(\omega,\boldsymbol{q}). \qquad [7]$$

Here, $V_{\boldsymbol{q}}=2\pi e^2/\kappa q$ is the Coulomb interaction in a medium with a background dielectric constant $\kappa$, and $\Pi(\omega,\boldsymbol{q})$ is the electron polarization function. The relation in Eq. **7** is exact as long as the polarization function is defined as an exact microscopic density–density pair correlator given by a sum of all irreducible bubble diagrams. As such, this relation can yield useful information about plasmon dispersion, even when electron interactions are strong.

Similar to the conventional analysis of plasmons in 2D systems, here a simplification occurs in the small-$q$ limit, regardless of whether the random-phase approximation (RPA) is used to evaluate $\Pi(\omega,\boldsymbol{q})$. Indeed, since the Coulomb potential diverges at small $q$, zeros of $\varepsilon(\omega,\boldsymbol{q})$ are found when the polarization function is small. However, at small $q$, this quantity vanishes as $\lambda q^2/\omega^2$, a behavior that is a consequence of the general symmetry requirements (namely, gauge invariance demanding that spatially uniform external potential does not perturb density) (31). This immediately yields a $q^{1/2}$ scaling for plasmon frequency at small-enough $q$.

Below, we use the RPA approach to estimate the prefactor $\lambda$ and to demonstrate that the mode $\omega\sim q^{1/2}$ extends far above the TBG p-h continuum. To compare with other systems, we recall the familiar "classical acceleration" behavior found for particles with parabolic dispersion: $\Pi(\omega,\boldsymbol{q})=nq^2/m\omega^2$, where $n$ is the charge density and $m$ is the electron band mass (31). For a more general band dispersion, the ratio $n/m$ is replaced by the band Fermi energy, $\lambda\sim E_F/\hbar^2$ (1–3). Interactions have no impact on the behavior of $\Pi(\omega,\boldsymbol{q})$ for the parabolic band case; however, for nonparabolic bands, the band mass $m$ must change to an effective value $m^*$ described by Landau Fermi-liquid renormalization (32).

In our case, the scaling relation $\Pi(\omega,\boldsymbol{q})\approx\lambda q^2/\omega^2$ features different values of $\lambda$ for low and high energies, $\omega\lesssim E_F$ and $\omega>2W$. To see this, we start with the RPA expression for polarization function

$$\Pi(\omega,\boldsymbol{q})=4\sum_{\boldsymbol{k},s,s'}\frac{(f_{s,\boldsymbol{k}+\boldsymbol{q}}-f_{s',\boldsymbol{k}})F^{ss'}_{\boldsymbol{k}+\boldsymbol{q},\boldsymbol{k}}}{E_{s,\boldsymbol{k}+\boldsymbol{q}}-E_{s',\boldsymbol{k}}-\omega-i0}. \qquad [8]$$

Here, summation $\sum_{\boldsymbol{k}}$ denotes integration over the Brillouin zone, the indices $s,s'$ run over the electron bands, and the factor of 4 in front of the summation accounts for the 4-fold degeneracy of the toy model. Here, $f_{s,\boldsymbol{k}}$ is the equilibrium distribution $1/(e^{\beta(E_{s,\boldsymbol{k}}-E_F)}+1)$, and $F^{ss'}_{\boldsymbol{k}+\boldsymbol{q},\boldsymbol{k}}$ describes band coherence factors. For our toy model,

$$F^{ss'}_{\boldsymbol{k}+\boldsymbol{q},\boldsymbol{k}}=|\langle\Psi_{s,\boldsymbol{k}+\boldsymbol{q}}|\Psi_{s',\boldsymbol{k}}\rangle|^2=\frac{1+ss'\cos(\varphi_{\boldsymbol{k}+\boldsymbol{q}}-\varphi_{\boldsymbol{k}})}{2}, \qquad [9]$$

where $\Psi_{s,\boldsymbol{k}}$ are pseudospinors given in Eq. **6**.

As we now show, an analytic expression for plasmon dispersion can be obtained, describing both the Landau-damped and the undamped cases in a unified way. We first rewrite Eq. **8** by performing a standard replacement $\boldsymbol{k}+\boldsymbol{q}\to-\boldsymbol{k}$ in the term containing $f_{s,\boldsymbol{k}+\boldsymbol{q}}$ followed by $-\boldsymbol{k}-\boldsymbol{q},-\boldsymbol{k}\to\boldsymbol{k}+\boldsymbol{q},\boldsymbol{k}$ justified by the $\boldsymbol{k}\to-\boldsymbol{k}$ time-reversal symmetry. This gives

$$\Pi(\omega,\boldsymbol{q})=8\sum_{\boldsymbol{k},s,s'}f_{s',\boldsymbol{k}}\frac{F^{ss'}_{\boldsymbol{k},\boldsymbol{k}+\boldsymbol{q}}(E_{s',\boldsymbol{k}}-E_{s,\boldsymbol{k}+\boldsymbol{q}})}{(E_{s,\boldsymbol{k}+\boldsymbol{q}}-E_{s',\boldsymbol{k}})^2-(\omega+i0)^2}. \qquad [10]$$

The behavior of this expression at small $q$, which will be of interest for us, can be found in a closed form. In the small-$q$ limit, the coherence factors behave as

$$F^{s=s'}_{\boldsymbol{k}+\boldsymbol{q},\boldsymbol{k}}\approx1,\quad F^{s=-s'}_{\boldsymbol{k}+\boldsymbol{q},\boldsymbol{k}}\approx\frac{1}{4}(\boldsymbol{q}\cdot\nabla_{\boldsymbol{k}}\varphi_{\boldsymbol{k}})^2. \qquad [11]$$

The values $O(1)$ for intraband transitions and $O(q^2)$ for interband transitions might suggest that the polarization function is dominated by the intraband transitions. However, as we now show, the interband and intraband contributions are of the same order of magnitude.

Indeed, the intraband contributions, $s=s'$, can be rewritten by noting that, on integration over $\boldsymbol{k}$, only the even-$\boldsymbol{k}$ part of series expansion $E_{s,\boldsymbol{k}+\boldsymbol{q}}-E_{s,\boldsymbol{k}}$ survives, giving $\Pi_1(\omega,\boldsymbol{q})\approx\frac{4}{\omega^2}\sum_{\boldsymbol{k},s}f_{s,\boldsymbol{k}}(E_{s,\boldsymbol{k}+\boldsymbol{q}}+E_{s,\boldsymbol{k}-\boldsymbol{q}}-2E_{s,\boldsymbol{k}})$. Expanding in small $q$, we have

$$\Pi_1(\omega,\boldsymbol{q})\approx\frac{4}{\omega^2}\sum_{\boldsymbol{k},s}f_{s,\boldsymbol{k}}(\boldsymbol{q}\cdot\nabla_{\boldsymbol{k}})^2E_{s,\boldsymbol{k}}. \qquad [12]$$

As a sanity check, for parabolic band $E_{\boldsymbol{k}}=k^2/2m$, we recover the familiar result $\Pi(\omega,\boldsymbol{q})=nq^2/m\omega^2$ (31).

The interband contributions, $s=-s'$, can be simplified by noting that $E_{s,\boldsymbol{k}+\boldsymbol{q}}\approx-E_{s',\boldsymbol{k}}$, giving

$$\Pi_2(\omega,\boldsymbol{q})\approx4\sum_{\boldsymbol{k},s}f_{s,\boldsymbol{k}}\frac{E_{s,\boldsymbol{k}}(\boldsymbol{q}\cdot\nabla_{\boldsymbol{k}}\varphi_{\boldsymbol{k}})^2}{4E_{s,\boldsymbol{k}}^2-(\omega+i0)^2}. \qquad [13]$$

As a sanity check, at $T=0$, the imaginary part of $\Pi_2$, describing interband transitions, is non-zero only for $2E_F<\omega<2W$ as

expected. The real part of $\Pi_2$ is negative at small $\omega$ and positive at large $\omega$, because the valence band contribution dominates over that of the conduction band.

Plasmon dispersion $\omega_p$ is given by the solution of the equation $\varepsilon(\omega, \boldsymbol{q}) = 0$ with $\Pi = \Pi_1 + \Pi_2$. Comparing the $\omega$ dependence of $\Pi_1$ and $\Pi_2$, we see that, at small frequencies $\omega < 2E_F$, the intraband contribution $\Pi_1$ dominates. This gives the dispersion in Eq. **1** with

$$\beta_q = \beta_0 + \beta_1 q + O(q^2), \qquad [14]$$

where the leading term $\beta_0 = 4\alpha v_F E_F/\hbar$ originates from $\Pi_1$ (*SI Appendix*, section 2), and the subleading $q$-dependent contribution is due to $\Pi_2$. The negative sign of $\Pi_2$ translates into $\beta_1 < 0$, softening the dispersion at low frequencies. This behavior, which holds the limit $\omega < 2E_F$, agrees with refs. 1, 2, and 27.

In the same manner, we can obtain the dispersion at high frequencies, $\omega > 2W$ (the intrinsically undamped regime). The analysis is again simplified by noting that, since $\alpha = e^2/\hbar\kappa v_F \gg 1$, the relevant values of $q$ are small compared with the Brillouin zone size, and thus, the small-$q$ limit considered above is sufficient to describe this behavior. Taking both the intraband and interband contributions in the asymptotic form $\Pi_1 = \lambda_1 q^2/\omega^2$, $\Pi_2 = \lambda_2 q^2/\omega^2$, where $\lambda_1 \approx 2E_F/\hbar^2\pi$, $\lambda_2 \approx 2(W - E_F)/\hbar^2\pi$ (*SI Appendix*, section 2), yields Eq. **1** with $\beta = \frac{2\pi e^2}{\kappa}(\lambda_1 + \lambda_2)$. The first term is identical to $\beta_0$ found at low frequencies, and the second term is of a positive sign, $\lambda_2 > 0$, describing stiffening of the plasmon dispersion due to interband transitions.

In the undamped regime, plasmon frequency peaks at $q$ values on the order of Brillouin zone scale. The peak value of $\omega_p$, given in Eq. **2**, can be found by estimating the energy differences $E_{s,\boldsymbol{k}+\boldsymbol{q}} - E_{s',\boldsymbol{k}}$ in Eq. **10** as $W$ and noting that the coherence band factor for large $q$ is in general nonvanishing and of order 1. This gives, for the practically interesting case of $E_F \sim W$, the result $\omega_p \sim \sqrt{\alpha} W$, which agrees with the dispersion $\omega_p = \sqrt{\beta q} = 2\sqrt{\alpha v_F W q/\hbar}$ provided that $\hbar v_F q$ saturates at $W$. Indeed, the estimated values of $\beta_0, \beta$ compared with the fitted curve in Fig. 1*A* (*SI Appendix*, section 2) indicate that $\omega_p = \sqrt{\beta_q q}$ relation from Eq. **1** is a good approximation for the plasmon dispersion at both small and large $q$.

The dielectric function of the 2-band toy model faithfully reproduces all of the qualitative features expected for the TBG band structure. However, we find that, despite matching the bandwidth $W$ and lattice period to those of TBG, the resulting plasmon dispersion extends to much higher energies then those that will be found below for the actual TBG band structure. This is simply because the 2-band model does not account for the effects of interband polarization of higher electron bands, which renormalize the dielectric constant down and soften the plasmon dispersion. We account for this in the toy model case by rescaling the effective fine structure constant such that the resulting plasmon dispersion is comparable in magnitude with the TBG result. Specifically, in Fig. 1*A*, we use an effective background dielectric constant $\kappa = 12.12$, which is 4 times larger than the dielectric constant $\kappa = 3.03$ corresponding to an air/TBG/hexagonal boron nitride (hBN) heterostructure.

Next, we turn to the analysis of plasmons in TBG flat bands at an experimentally relevant magic angle value $\theta = 1.05^\circ$ (16–18). To accurately describe the TBG band structure and eigenstates, we use the effective continuum Hamiltonian $H_{TBG}$ introduced in ref. 33. The full discussion of the band structure details can be found in *SI Appendix*, section 3; here, we only discuss 2 relevant energy scales: flat-band bandwidth $W$ and the gap $\Delta$ between the flat bands and the rest of the band structure. With regard to $W$ value, we note that, technically, the bandwidth of the flat bands, as predicted by the continuum mode $H_{TBG}$, is on the order of $W \approx 3.75$ meV. However, the bandwidth scale relevant for the interband and intraband excitations is actually closer to $\tilde{W} \approx 2$ meV, because most of the states in the band lie below 2 meV. In addition, since the states with energies outside $-2\,\text{meV} < E < 2\,\text{meV}$ are small $k$, their contribution to polarization function (Eqs. **12** and **13**), evaluated at small $q$, is small. We also note that, while the bandgap as predicted by the continuum model is $\Delta \approx 11.75$ meV, the actual gap size is still a subject of debate (34).

The definition of the polarization function for this TBG Hamiltonian is essentially identical to that of the tight-binding toy model (Eq. **8**). Now, however, we must account explicitly for the valley and spin degrees of freedom, for a larger number of electron bands, and for different coherence factors. Accordingly, we promote the band indices $s, s'$ in Eq. **8** to composite labels $n, m$, which label all electron bands, spins $\sigma$, and valleys $\xi$; this makes the additional factor of 4 in front of Eq. **8** redundant. The toy model coherence factors are replaced by the TBG coherence band factors $F^{nm}_{\boldsymbol{k}+\boldsymbol{q},\boldsymbol{k}}$, which are given by

$$F^{nm}_{\boldsymbol{k}+\boldsymbol{q},\boldsymbol{k}} = \left| \int_\Omega d^2 r \, \Psi^\dagger_{n,\boldsymbol{k}+\boldsymbol{q}}(\boldsymbol{r}) e^{i\boldsymbol{q}\cdot\boldsymbol{r}} \Psi_{m,\boldsymbol{k}}(\boldsymbol{r}) \right|^2, \qquad [15]$$

where $\Psi_{n,\boldsymbol{k}}(\boldsymbol{r})$ are the Bloch wavefunctions for momentum $\boldsymbol{k}$ and band/valley/spin composite label $n$, which diagonalize the continuum Hamiltonian (*SI Appendix*, section 3). The integral in Eq. **15** is carried over the moiré unit cell $\Omega$.

After the polarization function is evaluated, we can determine the dielectric function and identify TBG's collective modes from poles of $1/\varepsilon(\omega, \boldsymbol{q})$ as above. An example of a TBG's dielectric function at approximately half-filling of the electron band, $E_F = 0.289$ meV, is shown in Fig. 3; fixed $q$ line cuts and zeros of $\varepsilon(\omega, \boldsymbol{q})$ are illustrated in *SI Appendix*, section 4. In discussing the figure, it is helpful to contrast it with the calculation for the hexagonal-lattice toy model shown in Fig. 1*A*. We again see a well-defined intrinsically undamped plasmon mode $\omega_p$ (red in Fig. 1*A*) positioned above the p-h continuum; the mode resides inside the band gap $2W < \omega_p < W + \Delta$, which peaks at $\hbar\omega_p \approx 8.5$ meV before decreasing and becoming almost flat $\hbar\omega_p \approx 6.5$ meV at large momenta. In agreement with the analytic considerations above, we see the interband continuum extending

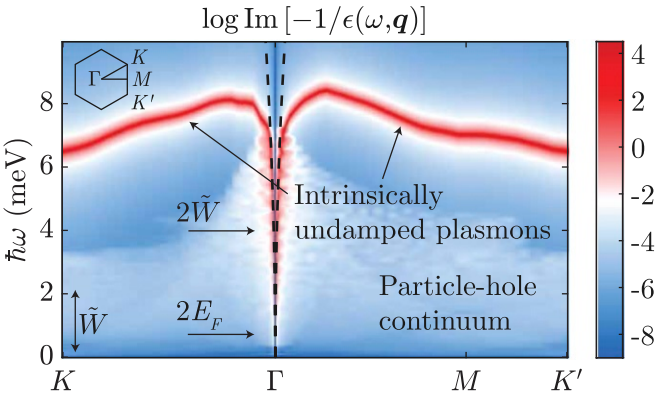


**Fig. 3.** Electron loss function $\text{Im}\,(-1/\varepsilon(\omega, \boldsymbol{q}))$ for TBG band structure. The Fermi energy value $E_F = 0.289$ meV corresponds to electron band half filling, and the average background dielectric constant is $\kappa = 3.03$ (typical of an air/TBG/hBN heterostructure). Log scale is used to clarify the relation between different features. Arrows mark the approximate interband p-h continuum edges obtained for the effective bandwidth $\tilde{W} \approx 2$ meV (see text). Plasmon dispersion (red line) at small $q$ is fitted with $\omega_p(q) = \sqrt{\beta_q q}$ (Eq. **1**) (dashed line), demonstrating a significant deviation from the typical 2D plasmon dispersion at large $q$. In the calculation, we used both flat bands and the next conduction/valence nonflat bands and verified that higher bands do not alter the quantitative and qualitative behavior.

from $2E_F$ to $2W$, but since $E_F = 0.289$ meV is extremely small, it makes the conventional (Landau-damped) part of plasmon dispersion $\omega < 2E_F$ invisible on the figure.

There are several unique aspects of the TBG plasmon dispersion compared with the behavior of generic narrow-band plasmons discussed above. To analyze the dispersion at $\omega_p > 2W$, we proceed just as in the toy model case, rewriting the TBG polarization function in a slightly different form of Eq. **10**, where the indices $n, m$ and the band coherence factor are modified as described above.

To proceed further analytically, we need to analyze Eq. **10** in the long-wavelength limit. However, unlike the 2-band toy model, where the only characteristic energy scale was the bandwidth $W$, the TBG band structure features an additional energy scale, namely, the gap between the flat bands and the rest of the energy spectrum. This impacts the small-$q$ series expansion of the polarization function, as now the energy difference $E_n - E_m$ between the occupied and unoccupied states can be larger than $\omega$. To account for such contributions in the series expansion, we split the summation over TBG bands into 2 parts, depending on whether $\omega$ or the energy difference $E_n - E_m$ is the largest energy scale in the denominator of Eq. **10**. This yields an approximate expression for the dielectric function

$$\varepsilon(\omega, \boldsymbol{q}) \approx 1 + A(\boldsymbol{q}) - \frac{B(\boldsymbol{q})}{\omega^2}, \qquad [16]$$

where we defined 2 auxiliary functions:

$$A(\boldsymbol{q}) = \frac{8\pi e^2}{\kappa q} \sum_{\boldsymbol{k},n,m}{}' f_{m,\boldsymbol{k}} \frac{F^{nm}_{\boldsymbol{k}+\boldsymbol{q},\boldsymbol{k}}}{E_{n,\boldsymbol{k}+\boldsymbol{q}} - E_{m,\boldsymbol{k}}} \qquad [17]$$

and

$$B(\boldsymbol{q}) = \frac{8\pi e^2}{\kappa q} \sum_{\boldsymbol{k},n,m}{}'' f_{m,\boldsymbol{k}} F^{nm}_{\boldsymbol{k}+\boldsymbol{q},\boldsymbol{k}} (E_{n,\boldsymbol{k}+\boldsymbol{q}} - E_{m,\boldsymbol{k}}). \qquad [18]$$

Here, the band summations $\sum'$ and $\sum''$ run over bands such that $\omega^2 > (E_{n,\boldsymbol{k}+\boldsymbol{q}} - E_{m,\boldsymbol{k}})^2$ and $\omega^2 < (E_{n,\boldsymbol{k}+\boldsymbol{q}} - E_{m,\boldsymbol{k}})^2$, respectively: for example, at large momenta, as seen in Fig. 3, the plasmon mode lies in the gap between the flat and nonflat bands, and hence, the $B(\boldsymbol{q})$ summation extends only over the flat bands, whereas the summation in $A(\boldsymbol{q})$ includes all of the remaining combinations of band indices. This allows us to write a closed form expression for the plasmon dispersion as

$$\omega_p^2 \approx \frac{B(\boldsymbol{q})}{1 + A(\boldsymbol{q})}, \qquad [19]$$

which must hold for both small and large $q$. We consider these 2 limits separately.

At small $q$, the matrix element of the Bloch wavefunctions, just as in the toy model case, favors the overlap between states from the same band. At the same time, there are fewer states in the $A(\boldsymbol{q})$ satisfying the condition $\omega^2 > (E_{n,\boldsymbol{k}+\boldsymbol{q}} - E_{n,\boldsymbol{k}})^2$, and hence, $A(\boldsymbol{q})$ vanishes for small $q$. This amounts to the plasmon dispersion $\omega_p$ from Eq. **19** reducing to $\omega_p^2 \approx B(\boldsymbol{q})$, and by comparison with Eq. **12**, we similarly expect a conventional 2D plasmon dispersion $\omega_p = \sqrt{\beta_q q}$ with $\beta_q$ given by the series from Eq. **14**. As we see in Fig. 3, the $\omega_p = \sqrt{\beta_q q}$ dispersion is a valid description only at very small $q$ compared with Fig. 1*A*, which can be traced back to higher bands softening the plasmon dispersion through the $A(\boldsymbol{q})$ term in Eq. **19**.

To determine how high the plasmon mode rises above the p-h continuum, we consider large $q$ values comparable with the reciprocal lattice vector. The arguments similar to those in the toy model show that, since $\alpha \gg 1$, we have $A(\boldsymbol{q}) \gg 1$. The dependence on the $e^2/\kappa q$ ratio, therefore, cancels between the $A(\boldsymbol{q})$ and $B(\boldsymbol{q})$ functions, resulting in the value of the plasmon dispersion $\hbar\omega_p \approx \sqrt{B(\boldsymbol{q})/A(\boldsymbol{q})} \sim \sqrt{W\Delta} \approx 6.6$ meV being dictated only by the continuum model's band structure parameters. This lack of explicit dependence on $\alpha$ suggests that, after the doping is such that $\alpha \gg 1$, the large-$q$ value of $\hbar\omega_p \approx \sqrt{W\Delta}$ becomes insensitive to doping (and hence, Fermi velocity). This behavior is different from that in the toy model, where $\omega_p \sim \sqrt{\alpha} W$ at large $q$. The relatively more weak dependence on $\alpha$ in the TBG case is due to interband polarization involving higher bands, which significantly alters the effective dielectric constant. The weak $q$ dependence at large $q$ is in agreement with the properties of interband plasmons described in ref. 19.

We also note that, although plasmons above the p-h continuum are kinematically protected from p-h excitation, which makes them undamped at the RPA level, there exist relaxation pathways through higher-order pair production in which several electron–hole pairs are emitted with total energy exceeding $\tilde{W}$, as well as phonon-assisted processes. For conventional plasmons these processes were analyzed in ref. 35. The role of these effects for plasmon lifetimes in TBG will be a subject of future work.

Before closing, we note that suppressing damping has always been central to the quest for tightly confined low-loss surface plasmon excitations. An early approach utilized surface electromagnetic modes traveling at the edge of an air/metal boundary (36), in which dissipation is low because most of the mode field resides outside the metal; however, the field confinement scale, set by optical wavelength, was fairly large. Next came surface plasmons propagating in high-mobility 2D electron gases in semiconductor quantum wells and monolayer graphene (14), which can provide deep-subwavelength confinement (3). However, plasmons in these systems are prone to a variety of dissipation mechanisms, with Landau damping usually regarded as the one that sets the fundamental limit on possible plasmon wavelengths and corresponding lifetimes. The possibility to overcome this fundamental limitation in narrow-band systems, such as moire graphene, creates a unique opportunity for graphene plasmonics. Damping-free plasmons can enable interference phenomena, dissipationless photon–matter coupling, and other interesting behaviors. It is also widely expected that low-dissipation plasmons can lead to unique applications for photon-based quantum information processing (15). Furthermore, reduced damping has more immediate consequences, as it translates into enhanced optical coherence that can be directly probed by scanning near-field microscopy, as discussed above, providing a clear signature of the undamped collective modes.

**ACKNOWLEDGMENTS.** We thank Ali Fahimniya for discussions. This work was supported, in part, by the Science and Technology Center for Integrated Quantum Materials, NSF Grant DMR-1231319, and Army Research Office Grant W911NF-18-1-0116.

1. B. Wunsch, T. Stauber, F. Sols, F. Guinea, Dynamical polarization of graphene at finite doping. *New J. Phys.* **8**, 318–318 (2006).
2. E. H. Hwang, S. Das Sarma, Dielectric function, screening, and plasmons in two-dimensional graphene. *Phys. Rev. B* **75**, 205418 (2007).
3. H. Buljan, M. Jablan, M. Soljačić, Damping of plasmons in graphene. *Nat. Photon.* **7**, 346–399 (2013).
4. J. Chen *et al.*, Optical nano-imaging of gate-tunable graphene plasmons. *Nature* **487**, 77–81 (2012).
5. Z. Fei *et al.*, Gate-tuning of graphene plasmons revealed by infrared nano-imaging. *Nature* **487**, 82–85 (2012).
6. E. J. Mele, Commensuration and interlayer coherence in twisted bilayer graphene. *Phys. Rev. B* **81**, 161405 (2010).
7. P. San-Jose, J. González, F. Guinea, Non-abelian gauge potentials in graphene bilayers. *Phys. Rev. Lett.* **108**, 216802 (2012).
8. R. Bistritzer, A. H. MacDonald, Moiré bands in twisted double-layer graphene. *Proc. Natl. Acad. Sci. U.S.A.* **108**, 12233–12237 (2011).

9. J. M. B. Lopes dos Santos, N. M. R. Peres, A. H. Castro Neto, Graphene bilayer with a twist: Electronic structure. *Phys. Rev. Lett.* **99**, 256802 (2007).
10. S. Fang, E. Kaxiras, Electronic structure theory of weakly interacting bilayers. *Phys. Rev. B* **93**, 235153 (2016).
11. T. Langer, J. Baringhaus, H. Pfnür, H. W. Schumacher, C. Tegenkamp, Plasmon damping below the landau regime: The role of defects in epitaxial graphene. *New J. Phys.* **12**, 033017 (2010).
12. F. J. G. de Abajo, Graphene plasmonics: Challenges and opportunities. *ACS Photon.* **1**, 135–152 (2014).
13. G. X. Ni *et al.*, Fundamental limits to graphene plasmonics. *Nature* **557**, 530–533 (2018).
14. A. Woessner *et al.*, Highly confined low-loss plasmons in graphene–boron nitride heterostructures. *Nat. Mater.* **14**, 421–425 (2014).
15. M. Gullans, D. E. Chang, F. H. L. Koppens, F. J. G. de Abajo, M. D. Lukin, Single-photon nonlinear optics with graphene plasmons. *Phys. Rev. Lett.* **111**, 247401 (2013).
16. Y. Cao *et al.*, Correlated insulator behaviour at half-filling in magic-angle graphene superlattices. *Nature* **556**, 80–84 (2018).
17. Y. Cao *et al.*, Unconventional superconductivity in magic-angle graphene superlattices. *Nature* **556**, 43–50 (2018).
18. M. Yankowitz *et al.*, Tuning superconductivity in twisted bilayer graphene. *Science* **363**, 1059–1064 (2019).
19. T. Stauber, H. Kohler, Quasi-flat plasmonic bands in twisted bilayer graphene. *Nano Lett.* **16**, 6844–6849 (2016).
20. F. Hu *et al.*, Real-space imaging of the tailored plasmons in twisted bilayer graphene. *Phys. Rev. Lett.* **119**, 247402 (2017).
21. N. K. Emani *et al.*, Electrically tunable damping of plasmonic resonances with graphene. *Nano Lett.* **12**, 5202–5206 (2012).
22. T. Low, P. Avouris, Graphene plasmonics for terahertz to mid-infrared applications. *ACS Nano* **8**, 1086–1101 (2014).
23. A. Principi, G. Vignale, M. Carrega, M. Polini, Bulk and shear viscosities of the two-dimensional electron liquid in a doped graphene sheet. *Phys. Rev. B* **93**, 125410 (2016).
24. M. Polini *et al.*, Plasmons and the spectral function of graphene. *Phys. Rev. B* **77**, 081411 (2008).
25. H. Yan *et al.*, Damping pathways of mid-infrared plasmons in graphene nanostructures. *Nat. Photon.* **7**, 394–399 (2013).
26. F. Stern, Polarizability of a two-dimensional electron gas. *Phys. Rev. Lett.* **18**, 546–548 (1967).
27. A. Principi, M. Polini, G. Vignale, Linear response of doped graphene sheets to vector potentials. *Phys. Rev. B* **80**, 075418 (2009).
28. M. Cohen, R. Shavit, Z. Zalevsky, Observing optical plasmons on a single nanometer scale. *Sci. Rep.* **4**, 4096 (2014).
29. H. Duan, A. I. Fernández-Domínguez, M. Bosman, S. A. Maier, J. K. W. Yang, Nanoplasmonics: Classical down to the nanometer scale. *Nano Lett.* **12**, 1683–1689 (2012).
30. E. A. Pashitskii, Plasmon mechanism of high-temperature superconductivity in cuprate metal-oxide compounds. *J. Exp. Theor. Phys. Lett.* **76**, 425–444 (1993).
31. G. Mahan, *Many-Particle Physics* (Springer US, Boston, 2000).
32. L. S. Levitov, A. V. Shtyk, M. V. Feigelman, Electron-electron interactions and plasmon dispersion in graphene. *Phys. Rev. B* **88**, 235403 (2013).
33. M. Koshino *et al.*, Maximally localized wannier orbitals and the extended hubbard model for twisted bilayer graphene. *Phys. Rev. X* **8**, 031087 (2018).
34. S. L. Tomarken *et al.*, Electronic compressibility of magic angle graphene superlattices. *Phys. Rev. Lett.* **123**, 046601 (2019).
35. E. G. Mishchenko, M. Y. Reizer, L. I. Glazman, Plasmon attenuation and optical conductivity of a two-dimensional electron gas. *Phys. Rev. B* **69**, 195302 (2004).
36. H. Raether, *Surface Plasmons on Smooth Surfaces* (Springer, Berlin, 1988), pp. 4–39.